Sub-Angstrom Characterization of Structural Origin for High In-Plane Anisotropy in 2D GeS_2

Xudong Wang,[1#] Jieling Tan,[1#] Chengqian Han,[1#] Jiang-Jing Wang,[1*] Lu Lu,[2] Hongchu Du,[3] Chun-Lin Jia,[2,3] Volker L. Deringer,[4*] Jian Zhou,[1] Wei Zhang[1,5*]

[1]Center for Advancing Materials Performance from the Nanoscale, State Key Laboratory for Mechanical Behavior of Materials, Xi'an Jiaotong University, Xi'an 710049, China
[2]The School of Microelectronics, State Key Laboratory for Mechanical Behavior of Materials, Xi'an Jiaotong University, Xi'an 710049, China
[3]Ernst Ruska-Centre for Microscopy and Spectroscopy with Electrons, Forschungszentrum Jülich GmbH, 52425 Jülich, Germany
[4]Department of Chemistry, Inorganic Chemistry Laboratory, University of Oxford, Oxford OX1 3QR, UK
[5]Xi'an Jiaotong University Suzhou Institute, Suzhou 215123, China

[*]Emails: wzhang0@mail.xjtu.edu.cn; jiangjingwang@mail.xjtu.edu.cn; volker.deringer@chem.ox.ac.uk

Abstract

Materials with layered crystal structures and high in-plane anisotropy, such as black phosphorus, present unique properties and thus promise for applications in electronic and photonic devices. Recently, the layered structures of GeS_2 and $GeSe_2$ were utilized for high-performance polarization-sensitive photodetection in the short wavelength region due to their high in-plane optical anisotropy and wide band gap. The highly complex, low-symmetric (monoclinic) crystal structures are at the origin of the high in-plane optical anisotropy, but the structural nature of the corresponding nanostructures remains to be fully understood. Here, we present an atomic scale characterization of monoclinic GeS_2 nanostructures and quantify the in-plane structural anisotropy at the sub-Angstrom level in real space by Cs-corrected scanning transmission electron microscopy. We elucidate the origin of this high in-plane anisotropy in terms of ordered and disordered arrangement of [GeS_4] tetrahedra in GeS_2 monolayers, through density functional theory (DFT) calculations and orbital-based bonding analyses. We also demonstrate high in-plane mechanical, electronic and optical anisotropies in monolayer GeS_2, and envision phase transitions under uniaxial strain that could potentially be exploited for non-volatile memory applications.

Keywords
germanium disulfide; complex 2D material; sub-Angstrom imaging; bonding mechanism; in-plane anisotropy

Two-dimensional (2D) materials beyond graphene are under active investigation, as they provide a rich platform to explore intriguing physical phenomena and to achieve applications in multi-functional and flexible devices.[1-4] As typical 2D semiconductors, transition metal dichalcogenides (TMDCs),[5] such as MoS_2, have a suitable electronic structure and hold great promises for diverse electronic and photonic applications, including field effect transistors,[6] photodetectors,[7] and memory devices.[8] Besides, physical phenomena such as valley polarization[9] and quantum spin Hall effects[10,11] have also been found in the 2D TMDCs. Similarly, layered main-group chalcogenides based on Ge and Sn have attracted much attention recently, due to their earth-abundant and environmentally friendly nature, thereby promising for sustainable applications.[12]

Elements of the fourth main group in the periodic table form both monochalcogenides and dichalcogenides with layered structures. Both these families can be physically exfoliated into 2D materials.[12] The ground state of group IV monochalcogenide monolayers, such as GeS, GeSe, SnS, and SnSe, shows a corrugated structure[13] that can be derived from the well-studied black phosphorus monolayer (phosphorene).[14] These materials have been predicted to possess multiferroic properties, with ferroelectric and ferroelastic order occurring simultaneously.[15] Later experiments have demonstrated that the SnTe monolayer is an in-plane ferroelectric material, which shows an unusual thickness scaling behavior.[16] Hence, these materials could potentially be used for future non-volatile memory[17] and non-linear optoelectronics[18] (owing to the breaking of centrosymmetry). SnS_2 and $SnSe_2$ have a simple 1T structure – the central Sn atoms are octahedrally coordinated by six outer S/Se atoms.[19] 2D SnS_2 and $SnSe_2$ in monolayer or few-layer form have been synthesized by chemical vapor deposition and incorporated into devices for various photonics applications.[20,21]

In comparison with SnS_2 and $SnSe_2$, the situation is more complicated for the germanium dichalcogenides, GeS_2 and $GeSe_2$. Although monolayers derived from the 1T structure, that is, with octahedral coordination of Ge, have been predicted to be dynamically stable by first-principles calculations,[22,23] the ground state of the two compounds favors a layered structure with tetrahedral coordination and much more complex structural patterns, containing 48 atoms in the bulk unit cell (space group $P2_1/c$).[24,25] In these structures, each layer is composed of 8 distorted, edge- and corner-sharing tetrahedral [GeS_4] and [$GeSe_4$] motifs in one unit cell. In comparison with rather simple local structural motifs of other 2D layered materials,[26] the atomic structure of the monoclinic phase is rather unconventional, making it more difficult to be discovered in automated, high-throughput screening.[26] A related case of a highly complex, yet experimentally

known and exfoliable structure is given by monoclinic Hittorf's phosphorus.[27]

It also remains unclear whether the structurally more complex germanium dichalcogenides can be easily exfoliated into monolayer form, and why such a free monolayer might be preferred over alternatives with structurally more simple arrangements. If this low-symmetric structural pattern can be retained in low-dimensional nanostructures, 2D GeS_2 and $GeSe_2$ are expected to show strong in-plane anisotropy in electrical, optical, and mechanical properties.[28] Indeed, nanoflakes of GeS_2 and $GeSe_2$ with a thickness of 4.2 nm and 3.5 nm were achieved recently *via* mechanical exfoliation,[29,30] and these materials were used as polarization-sensitive photodetectors in the short wave region, as their band gaps (> 2.5 eV) are larger than that of phosphorene (~1.0 eV).[14,31]

In this work, we carry out direct atomic-scale structural characterization of 2D GeS_2 nanostructures by means of Cs-corrected scanning transmission electron microscopy (STEM), allowing us to visualize and quantify the high structural anisotropy of monoclinic ("m-") GeS_2 in real space. Complementary, dispersion-corrected density functional theory (DFT) calculations suggest a small binding energy between the m-GeS_2 layers, corroborating the exfoliable nature of m-GeS_2. In addition, our DFT calculations predict high in-plane electrical, optical and mechanical anisotropies of m-GeS_2 in its monolayer form. In comparison with the more symmetric high-pressure phase of GeS_2 (HgI_2-type),[32] we elucidate the origin of the high in-plane anisotropy in the atomic structure and physical properties of m-GeS_2 through orbital-based bonding analyses. We also propose potential memory applications of 2D GeS_2 under uniaxial strain.

Results and Discussions

The samples for experimental investigations are powder of m-GeS_2 (commercially available at Chengdu Alfa Metal Material Co. Ltd). Scanning electronic microscopy (SEM) imaging showed that the sample was composed of micrometer-sized particles. Energy-dispersive X-ray (EDX) analysis confirmed the homogenous elemental distribution of Ge and S and the chemical composition close to the stoichiometry of GeS_2 (Figure S1). Figure 1a displays the SEM image of a typical particle. The particle looks compact along the planar directions, but shows weakly coupled layers with visible structural gaps along the vertical direction. These observed features are consistent with the crystal structure of m-GeS_2 (Figure 1b),[24,25] where no strong covalent interactions between the atomic layers can be expected, and with the previously observed cleavage behavior of the material.[25] Figure 1b also highlights the [GeS_4] tetrahedra as the characteristic building units in the material, which are linked in various ways *via* corners and edges, and the chemical nature of this linkage will be explored below. Lattice parameters of a = 6.80 Å, b = 16.29 Å, c = 11.68 Å and β = 91.20°, were obtained with dispersion-corrected DFT relaxations, in good agreement with X-ray diffraction experiments.[24,25] The calculated energy for exfoliation

of m-GeS_2 is 11 meV/Å^2 (Figure 1c). This value is notably smaller than that for 2H MoS_2 (21 meV/Å^2),[26] indicating the feasibility of exfoliation into monolayers.

The structure of the powder sample is firstly investigated by electron diffraction analysis. The recorded diffraction pattern along the normal of the a-b plane fits very well to the simulated one based on the DFT-relaxed atomic model of m-GeS_2 (Figure S2). To assess the atomic details of the m-GeS_2 structure, we carried out STEM characterization on the edge of the m-GeS_2 particle, where the thickness was small and suitable for high-resolution STEM investigation. Figure 2a shows the high angle annular dark field (HAADF) image of m-GeS_2 viewed along the normal of the a-b plane. The intensity of the HAADF image is roughly proportional to Z^2 (Ref.[33]), where Z represents the average atomic number of the atomic column along the view direction. Since the atomic number of Ge (Z = 32) is much larger than that of S (Z = 16), the bright dots represent the positions of the columns including the Ge atoms. During STEM investigation, effects of beam irradiation damage was observed, which led usually to a local dark contrast of the image (Figure 2a). Such effects is limited in causing any visible change of structural pattern, and can be avoided by adjusting the beam intensity properly (Figure S3). Statistical STEM investigations confirm that the GeS_2 sample is in a single monoclinic phase (Figures S3 and S4).

Figure 2b shows a zoomed-in HAADF image, which was averaged along the vertical direction over a damage-free part of the HAADF image to improve the signal-to-noise ratio and avoid the effect of beam damage. In most cases, the pure S atomic columns are invisible due to the very low signal. An exception are the S columns that have higher atom density and show faint contrast, as denoted by white arrows in Figure 2b. From the HAADF image, the structural feature of m-GeS_2 can be considered to be composed of two trapezoid-like building blocks arranged in opposite directions, which are marked by the red dashed lines in the image and correspondingly in the structure model of Figure 2c. In the structure model of Figure 2c the Ge atoms are accentuated by weakening the symbols of the S atoms (dashed line circles) for a clear comparison with the pattern of the HAADF image. Inside a structure block, the eight prominently bright dots correspond to the eight columns including Ge atoms. The positions of the S atomic columns are further confirmed on the annular bright-field (ABF) images (Figure S5), which reveals positions of both Ge and S atom columns.

To make a side by side comparison between the HAADF images and DFT calculations, we performed STEM image simulations[34] based on our DFT-relaxed atomic model. As shown in the inset of Figure 2b, the simulated HAADF image appears almost identical with the experimental one. The simulated image was obtained for a sample thickness of 20 nm. The typical distances between various Ge columns are given in the model in Figure 2c. These atomic scale images unambiguously verify the in-plane structural anisotropy of m-

GeS_2 along the x- and y-directions in low-dimension. We exposed the sample to air for more than one year, and repeated the STEM experiments on it. The obtained results demonstrated the excellent air-stability of m-GeS_2.

Next, we performed comprehensive DFT calculations on monolayer and multilayer 2D GeS_2. As shown in Figure 3a, the relaxed m-GeS_2 monolayer retains its bulk structural parameters with a_m = 6.80 Å, b_m= 16.30 Å and θ_m = 90°. Albeit the monoclinic crystal system refers to three-dimensional structures, we denote the resulting structure as "m-GeS_2 monolayer" for the sake of consistency. Our crystal orbital Hamilton population (COHP)[35-37] chemical bonding analyses support good chemical stability of the m-GeS_2: there is no antibonding orbital interaction in the valence bands (Figure 3b). In order to examine the dynamical stability of the monolayer, we performed phonon spectrum calculations and observed no imaginary frequencies (Figure 3c). In addition, we explore its electronic properties by calculating the density of states (DOS) (Figure 3b) and band structure (Figure 3d). We found that the m-GeS_2 monolayer is a direct band gap semiconductor. The band gap was calculated to be 2.45 eV using generalized gradient approximation functionals (Figure 3d) and 3.64 eV using hybrid functionals (Figure S6a). The latter value is close to the experimental data (3.71 eV) measured for a 2D nanoflake.[29] This direct-gap feature is retained in multilayer m-GeS_2 up to six-layer thickness in our simulations (Figure S7). Note that the extensively studied direct-gap monolayers, such as MoS_2 (~1.8 eV),[38] are typically narrow-gap semiconductors (< 2 eV), while m-GeS_2 enriches this material class with a much wider band gap.

Since the structural anisotropy in the material arises from the distorted and misaligned [GeS_4] tetrahedra, we also consider a possible competing structure of high symmetry: a GeS_2 monolayer in which all tetrahedra are connected *via* corners, resulting in a much more ordered arrangement (Figure 3e). This structure corresponds to a single slab of the high-pressure, layer-structured, tetragonal HgI_2-type phase[32] (Figure S8). We relaxed the simulation cell for this "t-GeS_2" monolayer while keeping the simple tetrahedral arrangement. The resulting metastable monolayer shows the lattice parameters of $a_t = b_t$ = 3.49 Å and θ_t = 90°, and an energy of 36 meV/atom, which is higher (less favorable) than that of the m-GeS_2 monolayer. Yet, the t-GeS_2 monolayer is both chemically and dynamically stable, as evidenced by its COHP data (Figure 3f) and phonon dispersion (Figure 3g). The calculated electronic DOS (Figure 3f) and band structure (Figure 3h) suggest t-GeS_2 to be an indirect semiconductor in monolayer form, with a gap size of 1.42 eV using a gradient-corrected DFT functional and 2.60 eV using a hybrid functional (Figure S6b).

We compare the primitive cell of the m-phase monolayer and a corresponding isoatomic 2 × 4 supercell of the t-phase monolayer (Figure 4a). For m-GeS_2, all inter-tetrahedral connections along the *x*-axis occur *via* corner sharing. Along the y-axis, in addition to

corner-sharing, there are two edges shared by four tetrahedra, namely, the edge between the 1st and 8th tetrahedra and the one between the 4th and 5th (in the numbering scheme of Figure 4a). The misaligned tetrahedra lead to a slightly reduced lattice parameter by 0.18 Å along the x-axis, but a much increased value by 2.34 Å along the *y*-axis, which result in a porous structure with ample free volume, making it a suitable candidate for high-performance sodium-ion battery anodes.[39] The structure of m-GeS_2 can, therefore, be seen as related to the SiS_2 type[40] where *all* tetrahedra share edges, as pointed out by Dittmar and Schäfer.[25] For t-GeS_2, in contrast, all the tetrahedra are linked by sharing corners.

To understand the bonding mechanisms, and to rationalize the energetic stability of the m-phase over the t-phase monolayer, we calculated the degree of charge transfer and the energy-integrated –COHPs for individual pairs of neighboring atoms (–ICOHP). These two analysis tools allow us to evaluate the strength of electrostatic and covalent interactions, respectively, in the two monolayers. The Löwdin charge analysis[41,42] gave almost identical charge transfer in both structures, with charges of about +0.44 |e| / –0.22 |e| on the Ge / S atoms, respectively, indicating a similar degree of ionic contributions to the bonding. Regarding the covalent character (Figure 4b), all bonds in t-GeS_2 are equivalent by symmetry; they therefore have the same length and the same –ICOHP value, and there is therefore only a single blue symbol in the distance-dependent plot of Figure 4b. However, there is a wide range of inequivalent bonds in m-GeS_2 and there, the value of –ICOHP changes as a function of bond length (red symbols in Figure 4b). In line with expectation, our analysis reveals the shortest bonds to be strongest; in particular, the –ICOHP values obtained for the shortest bonds indicate higher stabilization than the corresponding values for t-GeS_2. These stronger and shorter bonds are found in the denser region of m-GeS_2, namely, for the 2nd, 3rd, 6th and 7th tetrahedra in the labeling scheme of Figure 4a, whereas the weaker and longer bonds appear in the structurally more open area. In short, stronger covalent interactions in the tilted tetrahedra appear to stabilize the m-GeS_2 monolayer. This distortion-induced stabilization mechanism is also found in multilayer and bulk phase calculations, and therefore, we conclude that the strong in-plane anisotropy and the porous structure is indepdent on the film thickness (Figure S9).

The structural complexity of the m-GeS_2 monolayer (in particular, the different features in *x*- and *y*-direction discussed above) results in a strong in-plane anisotropy of various application-relevant physical properties. The ample open area in the monolayer may have direct impact on its mechanical response. In Figure 4, we present the calculated in-plane stiffness *C* along an arbitrary direction θ with the following equation:

$$C(\theta) = \frac{C_{11}C_{22} - C_{12}^2}{C_{11}sin^4\theta + C_{22}cos^4\theta + \left(\frac{C_{11}C_{22} - C_{12}^2}{C_{44}} - 2C_{12}\right)cos^2\theta sin^2\theta}$$

θ is the angle made with the positive *x*-direction in the *xy*-plane, and C_{ij} are the conventional elastic constants in the Voigt notation. The highest and lowest stiffness values are found along the *x*- and *y*-axis, respectively, with C_{11} = 29.7 N/m and C_{22} = 18.6 N/m, giving a high anisotropy ratio of 1.6. Such mechanical feature remains in the multilayer form (Figure S10). The small in-plane stiffness of m-GeS_2, in particular along the y-axis, suggest the m-GeS_2 monolayer to be mechanically rather soft, as compared to the stiffness of the more compact t-GeS_2 monolayer (78.5 N/m) and the rigid MoS_2 monolayer (180 N/m).[43] Given the presence of similar coordination environments, we speculate that potential phase transitions might take place between the m- and t-phase monolayers through the rearrangement of GeS_4 tetrahedra upon uniaxial strain engineering.

We also consider the optical absorption anisotropy of m-GeS_2 monolayer. The optical absorbance was calculated from the dielectric function based on the independent particle approximation, using the expression:

$$A(\omega) = 1 - \exp\left(-\frac{\omega}{c}\varepsilon^{(2)}d\right)$$

where *c* is the speed of light, $\varepsilon^{(2)}$ is the imaginary part of dielectric function, and *d* is the thickness of the simulation cell.[17] As shown in Figure 4d, a clear splitting of optical absorbance appears in the ultraviolet region. We also made an estimate about the optical absorbance of multilayer GeS_2, which shows a clear splitting and a high absorption rate of ~80% near the 250 nm wavelength region (Figure S11), comparing well with the device data based on a GeS_2 flake of similar thickness (~20 nm).[29] The *x*- and *y*-direction absorption spectra indicate the absorption under *x*-polarized and *y*-polarized light illumination. In contrast, due to its highly ordered structure, the t-GeS_2 monolayer is predicted to show isotropic optical absorbance in the ultraviolet region (Figure S12).

The potential structural transition should also be accompanied by an electronic transition from a direct-gap to an indirect-gap semiconductor with a change in band gap value by 1 eV (Figure 3 and S6), implying a notable change in electrical resistance. Moreover, the transport type should change from anisotropic to isotropic upon such structural transition. Based on the band structure presented in Figure 3d, we calculate the electron/hole effective mass along the Γ-X and Γ-Y directions according to the top valence band and the bottom conduction band. The results are 0.265 m_0 (*x*-axis) and 1.517 m_0 (*y*-axis) for electrons and 1.126 m_0 (*x*-axis) and 1.736 m_0 (*y*-axis) for holes, giving an in-plane ratio of 5.7 for electrons and 1.5 for holes. Here m_0 is the free electron mass. These data indicate a high in-plane anisotropic charge mobility in m-GeS_2 monolayer. In contrast, for the t-

GeS_2 monolayer, isotropic charge transport is expected, as the in-plane ratio is calculated to be 1, with an effective mass of 0.338 m_0 for electrons and 2.713 m_0 for holes.

Conclusion

In conclusion, we directly visualized the atomic structure of m-GeS_2 with sub-Angstrom resolution and quantified its structural anisotropy in real space. We elucidated the atomic origin of the complex structural pattern to be the stabilization of chemical bonds upon tilting of the corner-shared GeS_4 tetrahedra along the x-axis in the compact segment of the m-GeS_2 monolayer. We also predicted high in-plane electrical, optical, and mechanical anisotropies in the m-GeS_2 monolayer, yet isotropic behavior in the t-GeS_2 monolayer. A structural transition accompanied by a drastic change in optical and electrical properties is predicted to occur under uniaxial strain due to the small in-plane stiffness of m-GeS_2. The tunable electronic structure and optical absorbance may render 2D GeS_2 a potential candidate for electronic and optical memory on flexible substrates, enriching the established family of group IV chalcogenides (predominantly, tellurides) that currently employs amorphous-crystalline transitions for memory and photonics applications.[44-46]

Methods

Materials and Characterizations. The TEM and SEM specimen were prepared using a GeS_2 powder sample (commercially avaiable from the Chengdu Alfa Metal Material Co. Ltd). The powder was dispersed into suspension in ethanol solvent with the help of a KH3200B supersonic cleaner. The suspension was then dropped on the standard TEM copper grids (with the radius of 3mm) or Si wafers and dried completely. The atomic-resolution HAADF (high angle annular dark field) and ABF (annular bright field) images, SAED (selected area electron diffraction) patterns, as well as the EDX (energy dispersive X-ray) spectroscopy experiments were performed on a JEOL ARM200F with probe aberration correctors, operated at 200 keV. The zoom-in HAADF image was averaged along the vertical direction, and the ABF images were filtered[47] to improve the signal-to-noise ratio. The simulated HAADF and ABF images were carried out using the software packages of Dr. Probe.[34] The accelerating voltage was set to 200 keV, and the aperture radius alpha was 25 mrad, and the detection range of HAADF detector was 80-250 mrad. The SAED simulations were carried out with CrystalMaker software. The SEM images were observed by a FEI Helios NanoLab DualBeam FIB (focused ion beam) system at 10 kV.

Computational Methods. Density functional theory (DFT) calculations were carried out using the Vienna *ab initio* simulation package (VASP)[48] and Quantum ESPRESSO (QE)[49] package with projector augmented-wave (PAW)[50] pseudopotentials within the generalized gradient approximations (GGA).[51] The electronic, optical and mechanical property calculations were done by using VASP, while the phonon calculations were conducted by density functional perturbation theory (DFPT)[52] method implemented in QE. To obtain more accurate bandgap values, the HSE06 hybrid functional calculations[53] were

also carried out. For all the DFT data presented in the main text, GGA functionals were used. Van der Waals correction using the DFT-D3[54] method was included for all calculations. The cut-off energy for plane-wave was set to 520 eV for VASP and 65 Ry for QE. For Monkhorst-Pack k-point meshes, we chose 7 × 3 × 4 for bulk GeS_2, 7 × 3 × 1 for monolayer and multilayer monoclinic-GeS_2, and 20 × 20 × 1 for monolayer tetragonal-GeS_2. We included more than 20 Å thick vacuum in the z-axis for the monolayer calculations. All structures were relaxed until the force was less than 0.01 eV $Å^{-1}$. The convergence criterion for electronic iterations was 10^{-7} eV. Density of states (DOS) and Crystal Orbital Hamilton Population (COHP) analyses were done by the LOBSTER[55] code. The relaxed atomic coordinates of monolayer and bulk GeS_2 are included in the Supporting Information. All the crystal structures were depicted using the VESTA software.[56]

Associated Content

Acknowledgment

W.Z. acknowledges the support of National Natural Science Foundation of China (61774123), 111 Project 2.0 (BP2018008) and the Science and Technology Department of Jiangsu Province (BK20170414). J.Z. acknowledges the support of National Natural Science Foundation of China (21903063 and 11974270). H.D. and C.J. acknowledge funding from Deutsche Forschungsgemeinschaft (DFG) within SFB 917 ("Nanoswitches"). V.L.D. acknowledges a Leverhulme Early Career Fellowship and support from the Isaac Newton Trust. The authors acknowledge the International Joint Laboratory for Micro/Nano Manufacturing and Measurement Technologies at Xi'an Jiaotong University.

Supporting Information

The Supporting Information will be available free of charge at https://pubs.acs.org.

Additional experimental and computational results and supplementary discussion, and relaxed atomic coordinates of structural models (PDF)

References

1. Novoselov, K. S.; Geim, A. K.; Morozov, S. V.; Jiang, D.; Zhang, Y.; Dubonos, S. V.; Grigorieva, I. V.; Firsov, A. A. Electric Field Effect in Atomically Thin Carbon Films. *Science* **2004,** *306*, 666—669.

2. Manzeli, S.; Ovchinnikov, D.; Pasquier, D.; Yazyev, O. V.; Kis, A. 2D Transition Metal Dichalcogenides. *Nat. Rev. Mater.* **2017,** *2*, 17033.

3. Li, L.; Yu, Y.; Ye, G. J.; Ge, Q.; Ou, X.; Wu, H.; Feng, D.; Chen, X. H.; Zhang, Y. Black Phosphorus Field-Effect Transistors. *Nat. Nanotechnol.* **2014,** *9*, 372—377.

4. Zhou, F.; Chen, J.; Tao, X.; Wang, X.; Chai, Y. 2D Materials Based Optoelectronic Memory: Convergence of Electronic Memory and Optical Sensor. *Research* **2019,** *2019*, 9490413.

5. Wang, Q. H.; Kalantar-Zadeh, K.; Kis, A.; Coleman, J. N.; Strano, M. S. Electronics and Optoelectronics of Two-Dimensional Transition Metal Dichalcogenides. *Nat. Nanotechnol.* **2012,** *7*,

699—712.
6. Radisavljevic, B.; Radenovic, A.; Brivio, J.; Giacometti, V.; Kis, A. Single-Layer MoS_2 Transistors. *Nat. Nanotechnol.* **2011,** *6*, 147—150.
7. Lopez-Sanchez, O.; Lembke, D.; Kayci, M.; Radenovic, A.; Kis, A. Ultrasensitive Photodetectors Based on Monolayer MoS_2. *Nat. Nanotechnol.* **2013,** *8*, 497—501.
8. Wang, M.; Cai, S.; Pan, C.; Wang, C.; Lian, X.; Zhuo, Y.; Xu, K.; Cao, T.; Pan, X.; Wang, B.; Liang, S.-J.; Yang, J. J.; Wang, P.; Miao, F. Robust Memristors Based on Layered Two-Dimensional Materials. *Nat. Electron.* **2018,** *1*, 130—136.
9. Schaibley, J. R.; Yu, H.; Clark, G.; Rivera, P.; Ross, J. S.; Seyler, K. L.; Yao, W.; Xu, X. Valleytronics in 2D Materials. *Nat. Rev. Mater.* **2016,** *1*, 16055.
10. Qian, X.; Liu, J.; Fu, L.; Li, J. Quantum Spin Hall Effect in Two-Dimensional Transition Metal Dichalcogenides. *Science* **2014,** *346*, 1344—1347.
11. Wu, S.; Fatemi, V.; Gibson, Q. D.; Watanabe, K.; Taniguchi, T.; Cava, R. J.; Jarillo-Herrero, P. Observation of the Quantum Spin Hall Effect up to 100 Kelvin in a Monolayer Crystal. *Science* **2018,** *359*, 76—79.
12. Zhou, X.; Zhang, Q.; Gan, L.; Li, H.; Xiong, J.; Zhai, T. Booming Development of Group IV-VI Semiconductors: Fresh Blood of 2D Family. *Adv. Sci.* **2016,** *3*, 1600177.
13. Wiedemeier, H.; von Schnering, H. G. Refinement of the Structures of GeS, GeSe, SnS and SnSe. *Z. Kristallogr.* **1978,** *148*, 295—304.
14. Liu, H.; Neal, A. T.; Zhu, Z.; Luo, Z.; Xu, X.; Tomanek, D.; Ye, P. D. Phosphorene: An Unexplored 2D Semiconductor with a High Hole Mobility. *ACS Nano* **2014,** *8*, 4033—4041.
15. Wang, H.; Qian, X. Two-Dimensional Multiferroics in Monolayer Group IV Monochalcogenides. *2D Mater.* **2017,** *4*, 015042.
16. Chang, K.; Liu, J.; Lin, H.; Wang, N.; Zhao, K.; Zhang, A.; Jin, F.; Zhong, Y.; Hu, X.; Duan, W.; Zhang, Q.; Fu, L.; Xue, Q.-K.; Chen, X.; Ji, S.-H. Discovery of Robust In-Plane Ferroelectricity in Atomic-Thick SnTe. *Science* **2016,** *353*, 274—278.
17. Zhou, J.; Xu, H.; Li, Y.; Jaramillo, R.; Li, J. Opto-Mechanics Driven Fast Martensitic Transition in Two-Dimensional Materials. *Nano Lett.* **2018,** *18*, 7794—7800.
18. Wang, H.; Qian, X. Ferroicity-Driven Nonlinear Photocurrent Switching in Time-Reversal Invariant Ferroic Materials. *Sci. Adv.* **2019,** *5*, eaav9743.
19. Pałosz, B.; Salje, E. Lattice Parameters and Spontaneous Strain in AX_2 Polytypes CdI_2, PbI_2 SnS_2 and $SnSe_2$. *J. Appl. Crystallogr.* **1989,** *22*, 622—623.
20. Su, G.; Hadjiev, V. G.; Loya, P. E.; Zhang, J.; Lei, S.; Maharjan, S.; Dong, P.; Ajayan, P. M.; Lou, J.; Peng, H. Chemical Vapor Deposition of Thin Crystals of Layered Semiconductor SnS_2 for Fast Photodetection Application. *Nano Lett.* **2015,** *15*, 506—513.
21. Huang, Y.; Sutter, E.; Sadowski, J. T.; Cotlet, M.; Monti, O. L. A.; Racke, D. A.; Neupane, M. R.; Wickramaratne, D.; Lake, R. K.; Parkinson, B. A.; Sutter, P. Tin Disulfide—An Emerging Layered Metal Dichalcogenide Semiconductor: Materials Properties and Device Characteristics. *ACS Nano* **2014,** *8*, 10743—10755.
22. Wang, J.; Ronneberger, I.; Zhou, L.; Lu, L.; Deringer, V. L.; Zhang, B.; Tian, L.; Du, H.; Jia, C.; Qian, X.; Wuttig, M.; Mazzarello, R.; Zhang, W. Unconventional Two-Dimensional Germanium

Dichalcogenides. *Nanoscale* **2018,** *10*, 7363—7368.
23. Rasmussen, F. A.; Thygesen, K. S. Computational 2D Materials Database: Electronic Structure of Transition-Metal Dichalcogenides and Oxides. *J. Phys. Chem. C* **2015,** *119*, 13169—13183.
24. Rubenstein, M.; Roland, G. A Monoclinic Modification of Germanium Disulfide GeS_2. *Acta Crystallogr., Sect. B: Struct. Sci., Cryst. Eng. Mater.* **1971,** *B27*, 505—506.
25. Dittmar, G.; Schäfer, H. Die Kristallstruktur von H.T.-GeS_2. *Acta Crystallogr., Sect. B: Struct. Sci., Cryst. Eng. Mater.* **1975,** *B31*, 2060—2064.
26. Mounet, N.; Gibertini, M.; Schwaller, P.; Campi, D.; Merkys, A.; Marrazzo, A.; Sohier, T.; Castelli, I. E.; Cepellotti, A.; Pizzi, G.; Marzari, N. Two-Dimensional Materials from High-Throughput Computational Exfoliation of Experimentally Known Compounds. *Nat. Nanotechnol.* **2018,** *13*, 246—252.
27. Schusteritsch, G.; Uhrin, M.; Pickard, C. J. Single-Layered Hittorf's Phosphorus: A Wide-Bandgap High Mobility 2D Material. *Nano Lett.* **2016,** *16*, 2975—2980.
28. Li, L.; Han, W.; Pi, L.; Niu, P.; Han, J.; Wang, C.; Su, B.; Li, H.; Xiong, J.; Bando, Y.; Zhai, T. Emerging In-Plane Anisotropic Two-Dimensional Materials. *InfoMat* **2019,** *1*, 1—20.
29. Yang, Y.; Liu, S. C.; Wang, X.; Li, Z.; Zhang, Y.; Zhang, G.; Xue, D. J.; Hu, J. S. Polarization-Sensitive Ultraviolet Photodetection of Anisotropic 2D GeS_2. *Adv. Funct. Mater.* **2019,** *29*, 1900411.
30. Yang, Y.; Liu, S. C.; Yang, W.; Li, Z.; Wang, Y.; Wang, X.; Zhang, S.; Zhang, Y.; Long, M.; Zhang, G.; Xue, D. J.; Hu, J. S.; Wan, L. J. Air-Stable In-Plane Anisotropic $GeSe_2$ for Highly Polarization-Sensitive Photodetection in Short Wave Region. *J. Am. Chem. Soc.* **2018,** *140*, 4150—4156.
31. Mao, N.; Tang, J.; Xie, L.; Wu, J.; Han, B.; Lin, J.; Deng, S.; Ji, W.; Xu, H.; Liu, K.; Tong, L.; Zhang, J. Optical Anisotropy of Black Phosphorus in the Visible Regime. *J. Am. Chem. Soc.* **2016,** *138*, 300—305.
32. Shimada, M.; Dachille, F. Crystallization of Amorphous GeS_2 and $GeSe_2$ under Pressure. *Inorg. Chem.* **1977,** *16*, 2094—2097.
33. Pennycook, S. J.; Nellist, P. D. *Scanning Transmission Electron Microscopy Imaging and Analysis*; Springer: New York, 2011.
34. Barthel, J. Dr. Probe: A Software for High-Resolution STEM Image Simulation. *Ultramicroscopy* **2018,** *193*, 1—11.
35. Dronskowski, R.; Blochl, P. E. Crystal Orbital Hamilton Populations (COHP): Energy-Resolved Visualization of Chemical Bonding in Solids Based on Density-Functional Calculations. *J. Phys. Chem.* **1993,** *97*, 8617—8624.
36. Deringer, V. L.; Tchougreeff, A. L.; Dronskowski, R. Crystal Orbital Hamilton Population (COHP) Analysis as Projected from Plane-Wave Basis Sets. *J. Phys. Chem. A* **2011,** *115*, 5461—5466.
37. Maintz, S.; Deringer, V. L.; Tchougreeff, A. L.; Dronskowski, R. Analytic Projection from Plane-Wave and PAW Wavefunctions and Application to Chemical-Bonding Analysis in Solids. *J. Comput. Chem.* **2013,** *34*, 2557—2567.
38. Splendiani, A.; Sun, L.; Zhang, Y.; Li, T.; Kim, J.; Chim, C. Y.; Galli, G.; Wang, F. Emerging Photoluminescence in Monolayer MoS_2. *Nano Lett.* **2010,** *10*, 1271—1275.
39. Li, C. C.; Wang, B.; Chen, D.; Gan, L.-Y.; Feng, Y.; Zhang, Y.; Yang, Y.; Geng, H.; Rui, X.; Yu, Y. Topotactic Transformation Synthesis of 2D Ultrathin GeS_2 Nanosheets toward High-Rate and High-Energy-Density Sodium-Ion Half/Full Batteries. *ACS Nano* **2020,** *14*, 531—540.

40. Zintl, E.; Loosen, K. Siliciumdisulfid, ein anorganischer Faserstoff mit Kettenmolekülen. *Z. Phys. Chem.* **1935,** *174A*, 301—311.
41. Löwdin, P. O. On the Non-Orthogonality Problem Connected with the Use of Atomic Wave Functions in the Theory of Molecules and Crystals. *J. Chem. Phys.* **1950,** *18*, 365—375.
42. Ertural, C.; Steinberg, S.; Dronskowski, R. Development of a Robust Tool to Extract Mulliken and Löwdin Charges from Plane Waves and Its Application to Solid-State Materials. *RSC Adv.* **2019,** *9*, 29821—29830.
43. Bertolazzi, S.; Brivio, J.; Kis, A. Stretching and Breaking of Ultrathin MoS_2. *ACS Nano* **2012,** *5*, 9703—9709.
44. Zhang, W.; Mazzarello, R.; Wuttig, M.; Ma, E. Designing Crystallization in Phase-Change Materials for Universal Memory and Neuro-Inspired Computing. *Nat. Rev. Mater.* **2019,** *4*, 150—168.
45. Ding, K.; Wang, J.; Zhou, Y.; Tian, H.; Lu, L.; Mazzarello, R.; Jia, C.; Zhang, W.; Rao, F.; Ma, E. Phase-Change Heterostructure Enables Ultralow Noise and Drift for Memory Operation. *Science* **2019,** *366*, 210—215.
46. Feldmann, J.; Youngblood, N.; Wright, C. D.; Bhaskaran, H.; Pernice, W. H. P. All-Optical Spiking Neurosynaptic Networks with Self-Learning Capabilities. *Nature* **2019,** *569*, 208—214.
47. Du, H. A Nonlinear Filtering Algorithm for Denoising HR(S)TEM Micrographs. *Ultramicroscopy* **2015,** *151*, 62—67.
48. Kresse, G.; Furthmüller, J. Efficient Iterative Schemes for *Ab Initio* Total-Energy Calculations Using a Plane-Wave Basis Set. *Phys. Rev. B* **1996,** *54*, 11169—11186.
49. Giannozzi, P.; Baroni, S.; Bonini, N.; Calandra, M.; Car, R.; Cavazzoni, C.; Ceresoli, D.; Chiarotti, G. L.; Cococcioni, M.; Dabo, I.; Dal Corso, A.; de Gironcoli, S.; Fabris, S.; Fratesi, G.; Gebauer, R.; Gerstmann, U.; Gougoussis, C.; Kokalj, A.; Lazzeri, M.; Martin-Samos, L.; *et al*. QUANTUM ESPRESSO: A Modular and Open-Source Software Project for Quantum Simulations of Materials. *J. Phys. Condens. Matter.* **2009,** *21*, 395502.
50. Perdew, J. P.; Wang, Y. Accurate and Simple Analytic Representation of the Electron-Gas Correlation Energy. *Phys. Rev. B* **1992,** *45*, 13244—13249.
51. Perdew, J. P.; Burke, K.; Ernzerhof, M. Generalized Gradient Approximation Made Simple. *Phys. Rev. Lett.* **1996,** *77*, 3865—3868.
52. Baroni, S.; de Gironcoli, S.; Dal Corso, A.; Giannozzi, P. Phonons and Related Crystal Properties from Density-Functional Perturbation Theory. *Rev. Mod. Phys.* **2001,** *73*, 515—562.
53. Paier, J.; Marsman, M.; Hummer, K.; Kresse, G.; Gerber, I. C.; Angyan, J. G. Screened Hybrid Density Functionals Applied to Solids. *J. Chem. Phys.* **2006,** *124*, 154709.
54. Grimme, S.; Antony, J.; Ehrlich, S.; Krieg, H. A Consistent and Accurate *Ab Initio* Parametrization of Density Functional Dispersion Correction (DFT-D) for the 94 Elements H-Pu. *J. Chem. Phys.* **2010,** *132*, 154104.
55. Maintz, S.; Deringer, V. L.; Tchougreeff, A. L.; Dronskowski, R. LOBSTER: A Tool to Extract Chemical Bonding from Plane-Wave Based DFT. *J. Comput. Chem.* **2016,** *37*, 1030—1035.
56. Momma, K.; Izumi, F. VESTA 3 for Three-Dimensional Visualization of Crystal, Volumetric and Morphology Data. *J. Appl. Crystallogr.* **2011,** *44*. 1272—1276.

Figure captions

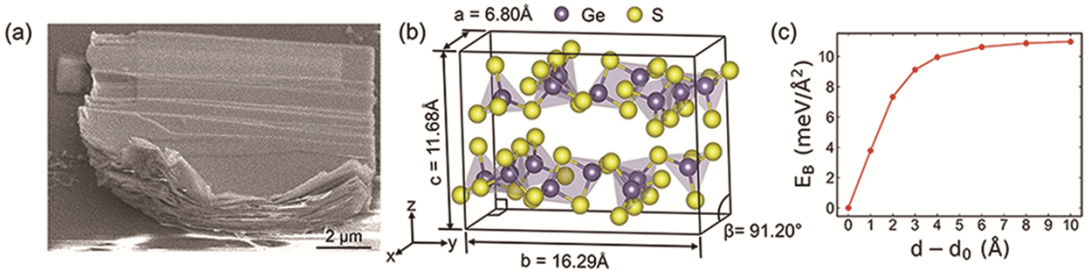

Figure 1. (a) SEM image of a typical m-GeS_2 particle. (b) Crystal structure of m-GeS_2. Ge and S atoms are rendered with purple and yellow spheres. All the [GeS_4] tetrahedra are visualized. (c) Computed binding energy E_B as a function of the separation distance between two separated parts, *i.e.*, exfoliating from the bulk structure (set as energy zero) to a free monolayer (which requires about 11 meV/Å^2).

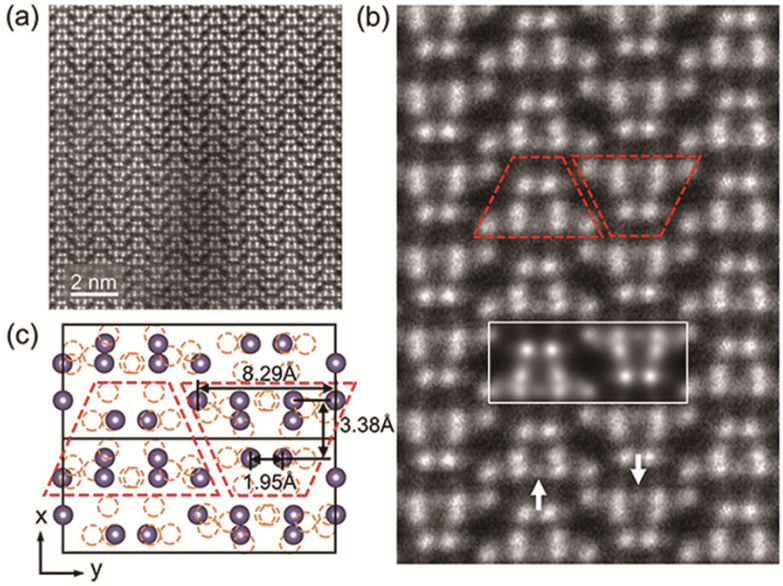

Figure 2. (a) A low magnification STEM-HAADF image. (b) A zoomed-in HAADF image, which is averaged along the vertical direction for improving the signal-to-noise ratio. White arrows denote the pure S atomic columns that show faint image contrast. Red dashed lines mark out the typical structure units. Inset shows the simulated HAADF image based on the DFT-relaxed model for sample thickness of 20 nm, which match excellently to the experimental image. (c) The bulk atomic structure (1 × 2 supercell) projected along the normal of the *a*-*b* plane. In the atomic model, Ge atoms are shown as purple spheres, whereas S atoms (which are less visible in the HAADF images) are shown as dashed yellow circles.

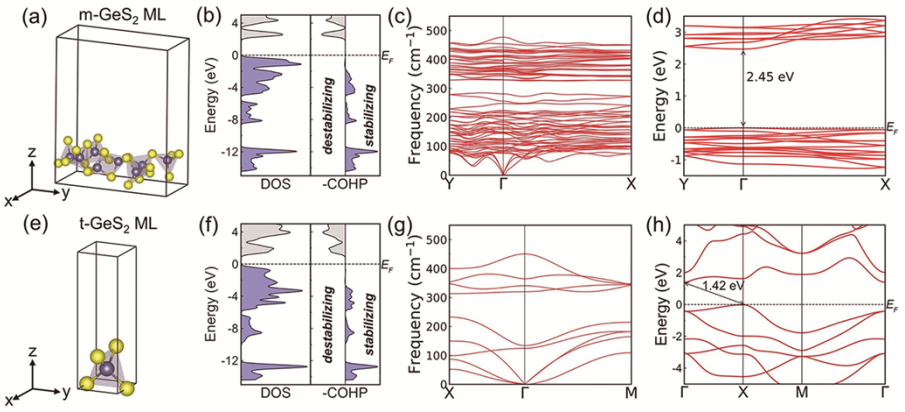

Figure 3. (a) The optimized atomic structure of m-GeS_2, shown in side view with the structure extending in the *x*- and *y*-directions. A vacuum region of 20 Å is added along the *z*-direction to simulate a monolayer, and the tetrahedral building units are highlighted similar to Figure 1b. (b–d) First-principles computation results for the m-GeS_2 monolayer, showing (b) DOS and COHP analysis of chemical bonding, (c) phonon dispersion curve, and (d) the electronic band structure (indicating the direct band gap at Γ). (e–h) The atomic structure, DOS and COHP, phonon dispersion curve and electronic band structure of t-GeS_2 monolayer.

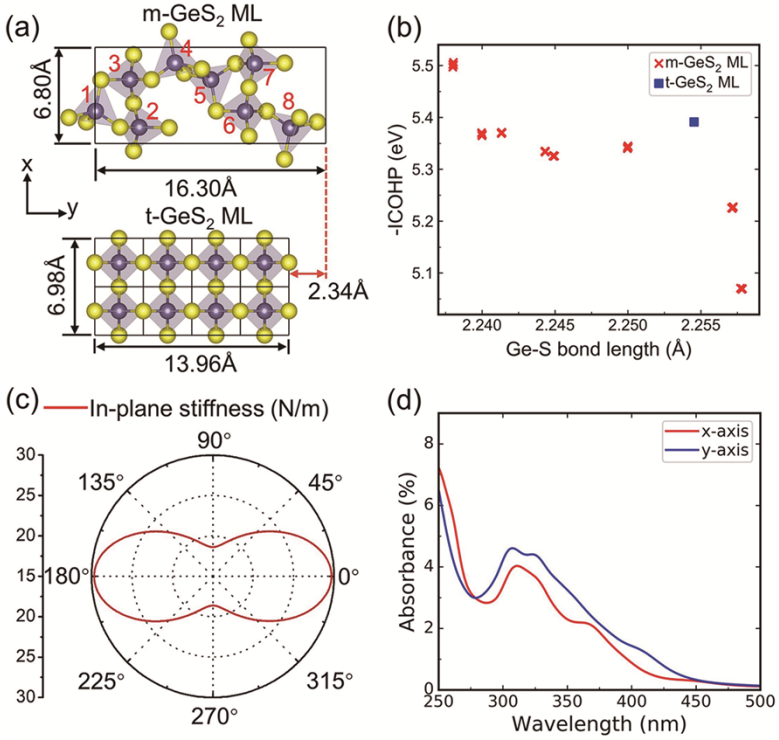

Figure 4. (a) The atomic structure of the m-GeS_2 (001) monolayer and a 2 × 4 supercell of the t-GeS_2 monolayer from the top view. (b) Bonding analyses of these two structures. (c) & (d) Calculated in-plane stiffness and optical absorbance of the m-GeS_2 monolayer.